IOP Publishing Plasma Sources Science and Technology
Plasma Sources Sci. Technol. **29** (2020) 09LT01 (6pp) https://doi.org/10.1088/1361-6595/abb21b

Letter

High-energy ballistic electrons in low-pressure radio-frequency plasmas

Yangyang Fu[1,2,5], Bocong Zheng[2,3], De-Qi Wen[1,2], Peng Zhang[2], Qi Hua Fan[2,3,4] and John P Verboncoeur[1,2]

[1] Department of Computational Mathematics, Science and Engineering, Michigan State University, East Lansing, Michigan 48824, United States of America
[2] Department of Electrical and Computer Engineering, Michigan State University, East Lansing, Michigan 48824, United States of America
[3] Fraunhofer Center for Coatings and Diamond Technologies, Michigan State University, East Lansing, Michigan 48824, United States of America
[4] Department of Chemical Engineering and Material Science, Michigan State University, East Lansing, Michigan 48824, United States of America

E-mail: fuyangya@msu.edu

Received 11 June 2020, revised 3 August 2020
Accepted for publication 24 August 2020
Published 6 October 2020

Abstract

This work demonstrates the presence of a small number of high-energy ballistic electrons (HEBEs) that originate from secondary electrons in low-pressure radio-frequency (rf) plasmas. The kinetic behaviors of the HEBEs are illustrated through electron energy probability functions from the fully kinetic particle-in-cell simulations, showing two wavy high-energy tails and two bifurcations during one rf cycle. Test-particle simulations and a semi-analytical method associated with nonlocal electron kinetics are performed to characterize the HEBE trajectories, which reveal the ballistic nature of the HEBEs and their typical bouncing features between the rf sheaths. Parameter dependence of the HEBEs on the discharge conditions (e.g., gas pressure, gap distance, and rf frequency) are identified, which is relevant to the plasma collisionality. With a pronounced presence of HEBEs, the overall impacts of the secondary electron emission on discharge parameters, such as electron power absorption and ionization rate, are also illustrated.

Keywords: RF plasma, ballistic electron, energetic electron, secondary electron, electron energy probability function, particle-in-cell simulation, nonlocal electron kinetics

(Some figures may appear in colour only in the online journal)

Low-pressure radio-frequency (rf) discharge plasmas have attracted attention for many years due to their widespread applications [1–3]. Among the focused studies, electron kinetics and heating mechanisms are of major interests, which are essential for the generation and control strategies of the rf plasmas [4–10]. It is generally recognized that in rf discharge plasmas, electrons are energized mainly through electrode-side stochastic (collisionless) heating at low pressure whereas bulk-region ohmic (collisional) heating becomes dominant at high pressure [11, 12]. Additional collisionless heating also exists in bounded rf plasmas when the bulk electrons are bounced back and forth between the oscillation sheaths at expanding phases, which is the so called bounce resonance heating (BRH) [13, 14]. The energized electrons, gaining energy from the sheath field and dissipating their energy to plasma through collisions, are of fundamental importance on the modulation of plasma properties.

[5] Author to whom any correspondence should be addressed.

Additional energetic electrons could be directly generated by secondary electron emissions (SEEs), which however are usually considered for high-pressure rf discharges in the *gamma*-mode where the ionization by electrons (e.g., secondary electrons) in the sheaths dominates. At low pressures, especially in the range of few mTorr, SEEs are often ignored for discharges in the *alpha*-mode where the ionization by electrons accelerated by the expanding sheaths dominates [15–17]. More recent studies incorporate various SEE mechanisms in low-pressure rf discharges and the impacts of SEEs on discharge parameters are investigated, with focuses on their roles in plasma control and parameter optimization [18–21]. Although the existence of ballistic beam electrons has been experimentally detected in rf plasmas at a certain pressure [22, 23], the kinetic behaviors of the energetic electrons and their parameter dependence on discharge conditions are still not fully demonstrated, leaving some of the underlying discharge features remain undiscovered.

In this work, we demonstrate the presence of a small number of high-energy ballistic electrons (HEBEs) that originate from secondary electrons in low-pressure rf plasmas. The energy trajectories of the HEBEs are illustrated through electron energy probability functions (EEPFs) obtained from particle-in-cell/Monte Carlo collision (PIC/MCC, 1d3v) simulations [24, 25]. Here we use the ASTRA code which was previously benchmarked with Turner *et al* [26] (see supplementary materials in [25] for the code benchmark and other details). The simulations are performed with argon at 300 K, accounting for three electron–neutral collisions (elastic, excitation, and ionization scattering) and two ion–neutral collisions (isotropic and backward scattering) [27]. The discharge is capacitively coupled and geometrically symmetric; the gas pressure p is $\leqslant$10 mTorr. The rf voltage $V_{\rm rf}(t) = 300 \cdot \sin(2\pi f t)$ (V), where $f = 1/T$ is the driving frequency with T being the rf period, is applied to electrode A (at $x = 0$) while electrode B (at $x = d$) is grounded. In the simulations, the time step is $\Delta t = T/1000$ and the grid size is $\Delta x = d/300$. The secondary electrons while considered are induced by the ion flux with an emission coefficient $\gamma_{\rm se} = 0.1$; the electron reflection probability is set to zero for all conditions. Test-particle simulations and a semi-analytical method associated with the nonlocal electron kinetics are performed to elucidate the HEBE behaviors. This work provides explicit demonstrations on the generation, kinetic information, and parameter dependence of HEBEs in low-pressure rf plasmas.

The temporal EEPF is calculated at the gap center when the discharge with SEE operates at the steady state, as shown in figure 1(a). The discharge condition is $(p, d, f) = (5$ mTorr, 5 cm, 13.56 MHz), which is considered as the base case in this work. It can be observed that the EEPF has two wavy high-energy tails and two bifurcations for each in one rf cycle, which are the trajectories of the named HEBE (justified later). This kind of EEPF has not been previously reported, probably owing to the neglected SEE at this rather low pressure and the limited energy scope in terms of the low-temperature plasmas. In figure 1(b) (zoomed from figure 1(a)), we can see that the lowest energy, corresponding to which the HEBE trajectory is still visible, is above ~60 eV, which remains much higher than

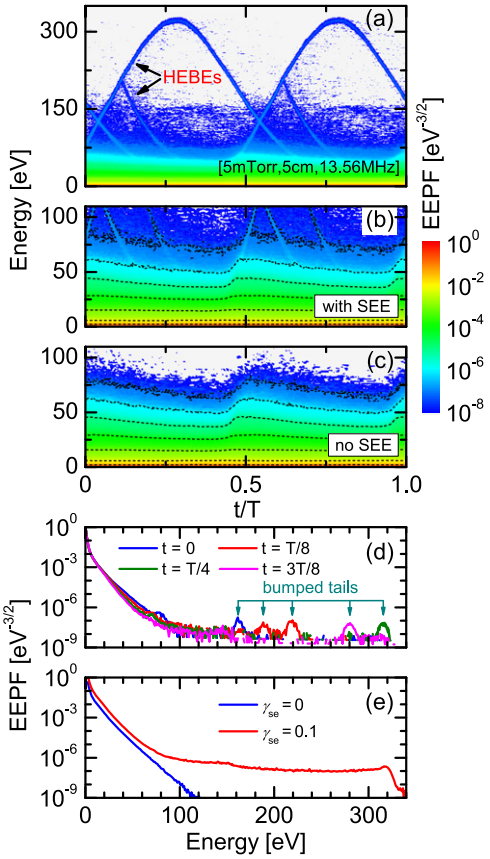

Figure 1. (a) Temporal EEPF with wavy high-energy tails and bifurcations, indicating the presence of HEBEs; (b) zoomed part of the EEPF with SEE; (c) temporal EEPF without SEE while other conditions are maintained; (d) EEPFs with SEE show bumped tails due to HEBE at different instants of time; (e) time-averaged EEPFs with and without SEE. In the simulation, $(p, d, f) = (5$ mTorr, 5 cm, 13.56 MHz).

the most energetic electrons (including the resonant electrons by BRH [14]) in low-temperature rf plasmas. In figure 1(c) with other conditions maintained but without SEE, the energy range of the EEPF is within 100 eV and the wavy high-energy tails no longer exist. In figures 1(b) and (c), the EEPFs are almost the same in the low-energy part, but strong differences are demonstrated for the high-energy region. It thus can be confirmed that the high-energy tails are caused by SEE and the HEBEs originate from the secondary electrons.

The existence of the energetic ballistic electrons was experimentally confirmed in the dc/rf hybrid capacitive coupled discharge and the energy distributions of the ballistic electrons were also diagnosed, but only accounting the electrons passing through the diagnostic window which can be detected by the energy analyzer [22]. The electron energy distribution function with a high-energy peak was also confirmed through test particle simulations, focusing only on emitted electrons [23]. In this work, we counted all the groups of the electrons at the gap center, thus the number of the HEBE is relatively small but clearly visible in the EEPF. Figure 1(d) shows the bumped high energy tails in the EEPFs, which indicates the small number of the HEBEs due to SEE at different instants of time (e.g., $t = 0, T/8, T/4$, and $3T/8$). The position and number of

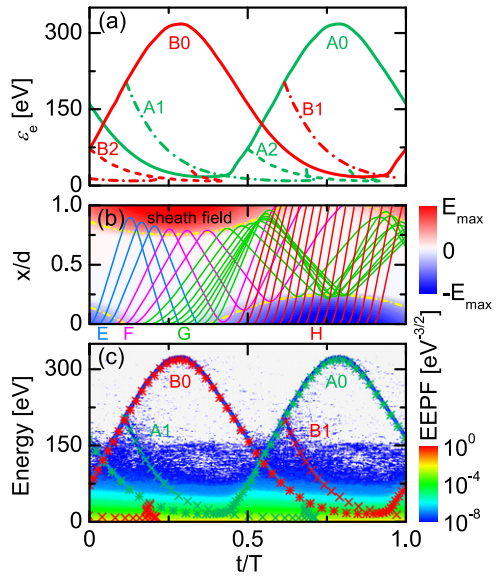

Figure 2. (a) Electron energy trajectories from test-particle simulations corresponding to the base case; (b) typical motion trajectories of electron emanating from electrode A ($x = 0$) at phases E, F, G, and H; spatiotemporal electric field is from the PIC simulation (E_{max} is 35.6 kV m^{-1}); (c) HEBE wavy trajectories in EEPF are exactly reproduced by A0, B0, A1, and B1 from the test-particle simulations.

the bumped tails are time-dependent, which is in accordance with the temporal HEBE trajectory in figure 1(a). Figure 1(e) shows the time-averaged EEPFs with and without SEE for $\gamma_{se} = 0.1$ and $\gamma_{se} = 0$, respectively. Without SEE the EEPF is bi-Maxwellian, having two distinct slopes, while with SEE it has a high-energy tail boosted up to about 320 eV, corresponding to the maximum potential of the rf sheath, of which the features also agree well previous PIC results [20, 28].

To elucidate the electron kinetics leading to the wavy trajectories observed in the EEPF, test-particle simulations are conducted based on the spatiotemporal electric field from the PIC results. The energy and time information of electrons are collected when they arrive at the gap center. The trajectories of the test-particles are shown in figure 2(a), where A0, A1, and A2 (green lines) are for electrons emanating from electrode A (at $x = 0$), and B0, B1 and B2 (red lines) are for electrons from electrode B (grounded). The numbers 0, 1, and 2 correspond to energy trajectories of electrons experiencing zero-, one-, and two-time bounces when detected at the gap center.

Since the discharge is symmetric, we only analyze the trajectories of electrons emanating from electrode A ($x = 0$). Typical electron motion trajectories during one rf cycle are represented by four groups of electrons emitted at phases E (one-time bounced), F (two-time bounced), G (three-time bounced), and H (without bouncing), as shown in figure 2(b). At the sheath collapsing phase (e.g., phases E, F, and G), the emitted electrons are weakly accelerated by the sheath fields and bounced back to the plasma bulk since they are not energetic enough to overcome the electrostatic potential well. At phase E, the electric field is still strong but decreasing and the emitted electrons at certain energy start being bounced, showing a bifurcated trajectory A1, which is descending when the first-bounced electrons from phases F and G having lower energy are also recorded in the following. At phase F, the emitted electrons having lower energy can bounce twice, corresponding to the bifurcated trajectory A2. At phase G, the emitted electrons can bounce more times and not discussed due to their relatively small energy. While emitted at phase H, the electrons are strongly accelerated and energetic enough to overcome the opposite sheath without bouncing. These electrons correspond to the right branch (i.e., $t/T > 0.45$) of the trajectory A0 while the left branch indicates the electrons from phases E, F, and G detected at the gap center before bouncing.

As shown in figure 2(c), the wavy trajectories of HEBE in EEPF are exactly reproduced by A0, B0, A1, and B1. The HEBEs in EEPF are composed of the electrons before their first bouncing or absorption (A0 and B0), which are detected during the whole rf cycle, and one-time bounced electrons (A1 and B1), which are detected at a certain time, especially when the sheath field is weak. The agreement of the energy trajectories from the test-particle and PIC simulations explicitly illustrates the ballistic nature of the HEBEs.

Figure 3 shows the parameter dependence of the HEBEs on the discharge conditions, including the gas pressure, gap distance, and rf frequency. Comparing to the base case (figure 1(a)), we find that a larger gap distance (see figure 3(a)) makes the HEBE less obvious whereas a higher rf frequency (see figure 3(b)) makes it more pronounced. From figures 3(a) and (c), we note that an increase of the gas pressure further weakens the HEBEs, even resulting in an absence of the trajectories of bounced electrons. The same pressure dependence can also be found in figures 3(b) and (d). The parameter dependence can be understood from the plasma collisionality, which can be characterized through two combined parameters pd and f/p. As shown in figures 4(a) and (b), although the individual parameters (p, d, f) are all different, the HEBE trajectories are maintained since pd and f/p are kept correspondingly the same. Physically, pd is proportional to the collision number in space ($pd \propto d/\lambda \sim N_{coll}$) while f/p represents an inverse of the collision number in time ($f/p \propto f/\nu_{coll} = T^{-1}/\tau_{coll}^{-1} \sim N_{coll}^{-1}$, where $\nu_{coll} = \tau_{coll}^{-1} \propto p$ is the electron collision frequency) [29–31]. The discharge with larger pd and smaller f/p is more collisional, in which the HEBEs have a high probability to experience energy-loss collisions and their ballistic nature is undermined. This is also consistent with the previous study for atmospheric pressure pure rare gas rf discharges (*gamma* mode) in which secondary electrons that have been accelerated in the sheath are short-lived and rapidly lose their energy due to the high collisionality [32, 33]. Note that the *gamma* modes at low pressure and high pressure may not be due to the same physical phenomenon; in molecular and rare gas mixtures the *gamma* mode at high pressure can be driven by secondary electrons as well as Penning ionization inside the sheaths [34, 35]. The moderate presence of HEBEs in figures 3(a) and (d) are also consistent with the intermediate values of pd and f/p, comparing to figures 4(b) and (c).

A semi-analytical method with the nonlocal electron kinetics is proposed to predict the HEBE trajectory without bouncing (see figure 3(c)). In the absence of energy-loss collisions, the total electron energy $\varepsilon_{tot} = \varepsilon_e - e\phi$ should be conserved,

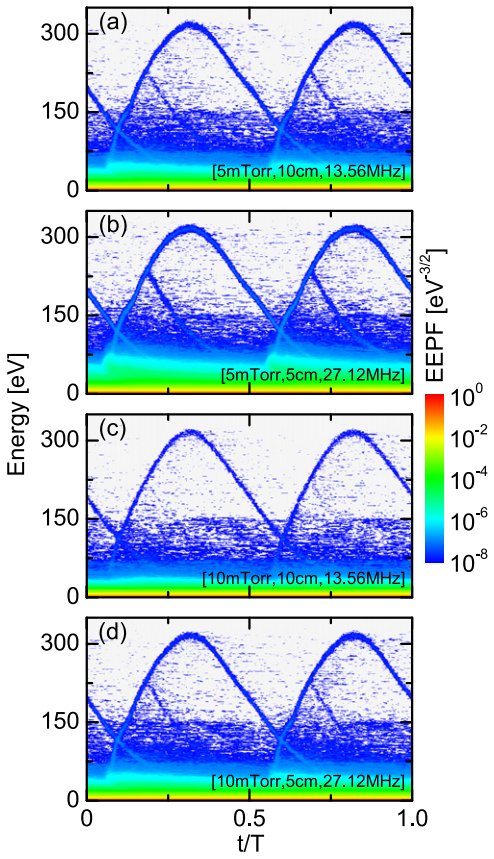

Figure 3. Parameter dependence of the HEBE in EEPF on the discharge condition parameters. (a) $(p, d, f) = (5$ mTorr, 10 cm, 13.56 MHz), (b) $(p, d, f) = (5$ mTorr, 5 cm, 27.12 MHz), (c) $(p, d, f) = (10$ mTorr, 10 cm, 13.56 MHz), and (d) $(p, d, f) = (10$ mTorr, 5 cm, 27.12 MHz).

where $\varepsilon_e = 1/2 m_e v_e^2$ is the kinetic energy (m_e is electron mass and v_e is velocity) and $\Phi = -e\phi$ is the potential energy [36]. The HEBE kinetic energy at the gap center thus can be estimated by the converted potential energy from the sheath potential. Figure 4(a) shows the electrode potentials ($\phi_A = V_{rf}$ and $\phi_B = 0$) and the potential differences between the gap center and the electrodes ($\Delta\phi_A = \phi_{x=d/2} - \phi_A$ and $\Delta\phi_B = \phi_{x=d/2} - \phi_B$). The converted potential energy of a secondary electron is detected as kinetic energy in the EEPF when they arrive at the gap center. Since the transit time inside the sheath is relatively short, during which the potential to kinetic energy conversion is complete, and the electrons travel at a constant velocity thereafter, the time delay for an electron transiting from the electrode to the gap center can be estimated by

$$\Delta t_\Phi \approx \frac{d}{2v_e} = \frac{d}{2\sqrt{2\varepsilon_e/m_e}} \tag{1}$$

The transit time depends on an electron kinetic energy (converted from the potential energy). Transforming the temporal potential difference and incorporating the transit time delay, the recorded kinetic energy of the electrons from electrode A and B is expressed as

$$\varepsilon_e(t) = e\Delta\phi'_{A,B}(t) = e\Delta\phi_{A,B}(t - \Delta t_\Phi). \tag{2}$$

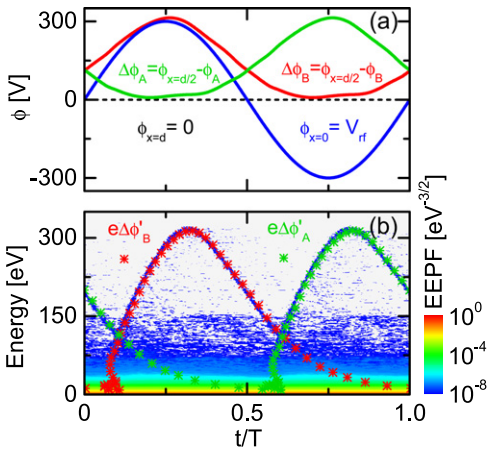

Figure 4. (a) Temporal electric potentials at electrodes A and B (ϕ_A and ϕ_B) and the potential differences between the gap center and the electrodes ($\Delta\phi_A$ and $\Delta\phi_B$); (b) HEBE trajectories predicted by the semi-analytical method show an excellent agreement with the PIC simulation. In the simulation, $(p, d, f) = (10$ mTorr, 10 cm, 13.56 MHz).

The HEBE trajectories predicted from equation (2) show an excellent agreement with the PIC simulation (see figure 4(b)), but only for the HEBEs before their first bouncing or absorption. As for the bounced HEBEs, their kinetic energy can also be modulated by the interacting sheath during bouncing and cannot be accurately estimated by their potential energy at the emanating electrode. Meanwhile, the energy of the bounce HEBEs is relatively lower and a small error may cause evident deviations on the trajectory prediction. Although only one case (cf: figure 3(c)) is demonstrated here, the semi-analytical method can also be applied for other cases to predict the HEBE wavy trajectories.

Figure 5 demonstrates the overall impact of SEE with a pronounced presence of the HEBEs on the discharge parameters. The SEE shows little impact on the electric potential while increases the electron density (~12%) in the bulk and the electron heating rate $P_e = \mathbf{J}_e \cdot \mathbf{E}$ (with $\mathbf{J}_e$ being the electron current density) in the sheath region (see figure 5(a)). The ionization is enhanced due to the turned-on SEE and the spatiotemporal ionization rate difference with and without SEE is calculated through $\Delta R_{iz}(x,t) = R_{iz}(x,t)_{SEE} - R_{iz}(x,t)_{noSEE}$, as shown in figure 5(b), which is generally positive during the whole rf cycle. The ionization enhancement is mostly pronounced inside the plasma bulk, especially on the bulk side of the sheath edge during the sheath expansion. The maximum ionization rate without SEE is $\sim 1.5 \times 10^{20}$ m^{-3}·s^{-1} and the ionization rate increase shown in figure 5(b) is about ten times smaller, which corresponds the percentage of the electron density increase (~12%). The enhanced ionization can be attributed to both the direct ionization from secondary electrons (including HEBEs) and their indirect effects. Figure 5(c) shows integrated ionization probabilities along the HEBE motion trajectories (see figure 2(b)), $S_{iz} = \sum_j \left(1 - \exp\left(-\sigma_{iz}(t_j) N_n v_e(t_j) \Delta t_j\right)\right)$, which reflect relative ionization abilities that could be directly from the secondary electrons. The ionization ability is strong either when the electron trajectory (or trapping time) is long (at phase G), or the electron energy is high (at phase H). The

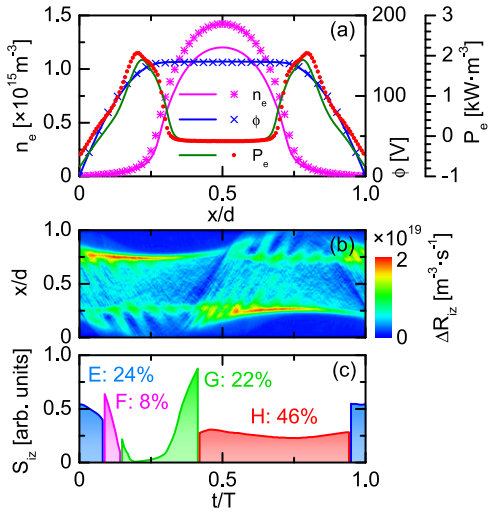

Figure 5. (a) Time-averaged electron density n_e, electric potential ϕ, and electron heating rate P_e for the base case (symbols are with SEE and solid lines are without SEE); (b) ionization rate increase due to the turned-on SEE; (c) integrated ionization probability S_{iz} along the HEBE motion trajectories.

electrons emitted at phase H, having the energy closely corresponding to the highest ionization cross section, show the highest percentage (∼46%) for contributing to the ionization. Note that although some of them may experience energy-loss collisions, the HEBEs alone cannot explain the ionization increase since they are mostly ballistic; other energetic electrons, such as the non-HEBE secondary electrons and 'cold' bulk electrons energized through interacting with energetic beam electrons [37, 38], also contribute. The electron heating through particle–field and particle–particle interactions can also be enhanced with the additional energetic beam electron from SEE. The indirect mechanism and direct impact of all the secondary electrons raise population of the high-energy tail in EEPF, enhancing the ionization in the rf plasmas.

In summary, we have demonstrated the presence of HEBEs originating from secondary electrons in low-pressure rf plasmas from the fully kinetic PIC simulations. It is found that the wavy HEBE trajectories (A0 and B0) in EEPF are composed of the electrons before their first bouncing or absorption, which are detected during the whole rf cycle; the trajectory bifurcation (A1 and B1) in EEPF is due to the one-time bounced electrons from the opposite electrode, which are detected during certain time phase. The presence of the HEBEs is identified to be relevant to the plasma collisionality, which is less pronounced when the combined parameter pd becomes larger or f/p becomes smaller. With a pronounced presence of HEBEs, the turned-on SEE shows little impact on the electric potential while increases the electron density, the electron power absorption, and the ionization. The enhanced ionization can be attributed to both the direct ionization from secondary electrons (including HEBEs) and their indirect effects, among which their relative ionization abilities are evaluated through the integrated ionization probability. This work explicitly demonstrated the generation, kinetic information, and parameter dependence of HEBEs, providing essential details for comprehensively understanding the electron kinetics in rf plasma devices. The influence of energy-dependent SEE on the presence of HEBEs will be incorporated in future work. One may also expect more complicated kinetic effects when electrodes are strongly emissive (thermionic surfaces [39, 40]) or externally ejected electrons are considered, which will also be the subjects of future work.

Acknowledgments

The authors are grateful to Professor Hae June Lee (Pusan National University) for his helpful comments and fruitful discussions. This work was supported by the Air Force Office of Scientific Research Grant FA9550-18-1-0062, the Air Force Office of Scientific Research Grant FA9550-18-1-0061, the U.S. Department of Energy Office of Fusion Energy Science Grant DE-SC0001939, and the National Science Foundation Awards #1917577 and #1724941.

ORCID iDs

Yangyang Fu https://orcid.org/0000-0001-9593-3177
Bocong Zheng https://orcid.org/0000-0002-6052-3693
De-Qi Wen https://orcid.org/0000-0002-2662-9777
Peng Zhang https://orcid.org/0000-0003-0606-6855
Qi Hua Fan https://orcid.org/0000-0002-8612-1326
John P Verboncoeur https://orcid.org/0000-0002-7078-3544

References

[1] Lieberman M A and Lichtenberg A J 2005 *Principles of Plasma Discharges and Material Processing* (New York: Wiley)
[2] Désangles V, Raimbault J L, Poyé A, Chabert P and Plihon N 2019 *Phys. Rev. Lett.* **123** 265001
[3] Bruneau B, Gans T, O'Connell D, Greb A, Johnson E V and Booth J P 2015 *Phys. Rev. Lett.* **114** 125002
[4] Godyak V A 2006 *IEEE Trans. Plasma Sci.* **34** 755
[5] Surendra M and Graves D B 1991 *Phys. Rev. Lett.* **66** 1469
[6] Kaganovich E B 1999 *Phys. Rev. Lett.* **82** 327
[7] Gozadinos G, Turner M M and Vender D 2001 *Phys. Rev. Lett.* **87** 135004
[8] Turner M M 2009 *J. Phys. D: Appl. Phys.* **42** 194008
[9] Mussenbrock T, Brinkmann R P, Lieberman M A, Lichtenberg A J and Kawamura E 2008 *Phys. Rev. Lett.* **101** 085004
[10] Wilczek S, Schulze J, Brinkmann R P, Donkó Z, Trieschmann J and Mussenbrock T 2020 *J. Appl. Phys.* **127** 181101
[11] Chabert P and Braithwaite N 2011 *Physics of Radio-Frequency Plasmas* (Cambridge: Cambridge University Press)
[12] Turner M M and Chabert P 2006 *Phys. Rev. Lett.* **96** 205001
[13] Park G Y, You S J, Iza F and Lee J K 2007 *Phys. Rev. Lett.* **98** 085003
[14] Liu Y X, Zhang Q Z, Jiang W, Hou L J, Jiang X Z, Lu W Q and Wang Y N 2011 *Phys. Rev. Lett.* **107** 055002
[15] Denpoh K and Ventzek P L G 2008 *J. Vac. Sci. Technol.* A **26** 1415
[16] Kawamura E, Lichtenberg A J and Lieberman M A 2008 *Plasma Sources Sci. Technol.* **17** 045002
[17] Donkó Z, Schulze J, Hartmann P, Korolov I, Czarnetzki U and Schüngel E 2010 *Appl. Phys. Lett.* **97** 081501

[18] Sun J Y, Zhang Q Z, Liu Y X and Wang Y N 2020 *Plasma Sources Sci. Technol.* **29** 024001
[19] Daksha M, Derzsi A, Wilczek S, Trieschmann J, Mussenbrock T, Awakowicz P, Donkó Z and Schulze J 2017 *Plasma Sources Sci. Technol.* **26** 085006
[20] Horváth B, Schulze J, Donkó Z and Derzsi A 2018 *J. Phys. D: Appl. Phys.* **51** 355204
[21] Derzsi A, Horváth B, Korolov I, Donkó Z and Schulze J 2019 *J. Appl. Phys.* **126** 043303
[22] Xu L, Chen L, Funk M, Ranjan A, Hummel M, Bravenec R, Sundararajan R, Economou D J and Donnelly V M 2008 *Appl. Phys. Lett.* **93** 261502
[23] Khrabrov A V, Kaganovich I D, Ventzek P L G, Ranjan A and Chen L 2015 *Plasma Sources Sci. Technol.* **24** 054003
[24] Verboncoeur J P, Alves M V, Vahedi V and Birdsall C K 1993 *J. Comput. Phys.* **104** 321
[25] Zheng B, Wang K, Grotjohn T, Schuelke T and Fan Q H 2019 *Plasma Sources Sci. Technol.* **28** 09LT03
[26] Turner M M, Derzsi A, Donkó Z, Eremin D, Kelly S J, Lafleur T and Mussenbrock T 2013 *Phys. Plasmas* **20** 013507
[27] Gudmundsson J T and Lieberman M A 2011 *Phys. Rev. Lett.* **107** 045002
[28] Diomede P, Kim D and Economou D J 2013 *AIChE J.* **59** 3214
[29] Fu Y, Zhang P, Verboncoeur J P and Wang X 2020 *Plasma Res. Express* **2** 013001
[30] Fu Y and Verboncoeur J P 2019 *IEEE Trans. Plasma Sci.* **47** 1994
[31] Lee M U, Lee J, Lee J K and Yun G S 2017 *Plasma Sources Sci. Technol.* **26** 034003
[32] Iza F, Lee J K and Kong M G 2007 *Phys. Rev. Lett.* **99** 075004
[33] Shi J J and Kong M G 2006 *Phys. Rev. Lett.* **96** 105009
[34] Liu D W, Iza F and Kong M G 2008 *Appl. Phys. Lett.* **93** 261503
[35] Liu D W, Iza F and Kong M G 2009 *Appl. Phys. Lett.* **95** 031501
[36] Tsendin L D 2010 *Phys.-Usp.* **53** 133
[37] Meige A, O'Connell D, Gans T and Boswell R W 2008 *IEEE Trans. Plasma Sci.* **36** 1384
[38] Wilczek S *et al* 2016 *Phys. Plasmas* **23** 063514
[39] Campanell M D and Umansky M V 2016 *Phys. Rev. Lett.* **116** 085003
[40] Campanell M D and Johnson G R 2019 *Phys. Rev. Lett.* **122** 015003